

# Decoherence analysis of silicon vacancies in 3C-SiC

Tommaso Fazio<sup>1,2</sup>, Giuseppe Fisicaro<sup>1</sup>, Ioannis Deretzis<sup>1</sup>,  
Elisabetta Paladino<sup>2,3,1</sup> and Antonino La Magna<sup>1</sup>

November 2, 2022

<sup>1</sup>) Consiglio Nazionale delle Ricerche, Istituto per la Microelettronica e Microsistemi (CNR-IMM), Z.I. VIII Strada 5, I-95121 Catania, Italy

<sup>2</sup>) Dipartimento di Fisica e Astronomia “Ettore Majorana”, Università di Catania, Via S. Sofia 64, I-95129 Catania, Italy

<sup>3</sup>) INFN Sezione di Catania, 95123 Catania, Italy

<sup>a</sup>tommaso.fazio@dfa.unict.it

## Abstract

We study the silicon vacancy in 3C-SiC as a color center of interest in the field of Quantum Technologies, focusing on its magnetic interaction with the SiC nuclear spin bath containing Si<sup>29</sup> and C<sup>13</sup> nuclei in their natural isotopic concentration. We calculate the system’s energetic and magnetic properties with ab initio methods based on the Density Functional Theory, identifying the neutral charge state of the silicon vacancy as the most favorable for p-doped 3C-SiC systems. We thereon evaluate the Free Induction Decay and the Hahn-echo sequence on the electron spin interacting with the nuclear spin bath. Here, the Electron Spin Echo Envelope Modulation phenomenon, due to single nuclear spin flipping processes, and the overall decay are highlighted in the context of the Cluster Correlation Expansion theory. We find a non-exponential coherence decay, which is a typical feature of solid-state qubits subjected to low frequency 1/f-type noise from the environment.

# 1 Introduction

Silicon carbide (SiC) is widely recognized as an interesting material for technological applications. Its capacity to work in harsh environments under high temperatures, yielding faster switching speeds, lower power losses and higher blocking voltages with respect to silicon has boosted its industrial exploitation in solid-state devices [1]. Within this context, SiC-based architectures have been already used as shields in accelerators [2], power devices in electronics [3] and quantum sensors of magnetic fields and temperature gradients [4]. The latter is just one of a number of different and emerging applications for SiC, which regard its use in Quantum Technologies (QT). Here, color centers generated by point-like defective configurations like divacancies or Si/C vacancies can provide the active states in which quantum information is encoded, processed and stored. Out of the many SiC polytypes, where the difference lies in the structure of the stacking layers, the most studied are the hexagonal 4H- and 6H-SiC [5] ones, due to the significant progress made in their epitaxial growth and the availability of high-quality samples. On the other hand, the cubic 3C-SiC polytype could potentially be an interesting and convenient alternative due to the possibility to be heteroepitaxially grown on silicon substrates, along with a series of physical characteristics which are appealing for electronic devices (lower band gap, absence of deep level stacking-fault defect states, higher electron and hole mobilities, etc.) [6, 7]. However, the low quality of 3C-SiC crystals during the past has largely hindered its technological use and slowed down its further theoretical study. Recently, the fabrication techniques and the control of defectivity for cubic 3C-SiC during growth processes have been greatly enhanced [7, 8]. Consequently, QT driven investigations dedicated to 3C-SiC based systems could raise an increasing interest in the near future as has happened for 6H- and 4H-SiC [9].

This study theoretically focuses on a point defect in 3C-SiC having a strong potentiality for QTs due to the low rate of quantum information loss [9, 10], even at room temperature [11]. In particular, we have considered the neutral and charged silicon vacancies ( $V_{\text{Si}}^0$ ,  $V_{\text{Si}}^{-1}$  and  $V_{\text{Si}}^{-2}$ ) magnetically interacting with the SiC nuclear spin bath, constituted by naturally occurring  $\text{Si}^{29}$  and  $\text{C}^{13}$  paramagnetic nuclei. Such system can be optically driven for coherent control purposes [4]. Furthermore, its energetics [12] and hyperfine interaction [13] properties can be calculated via *ab initio* methods based on the Density Functional Theory (DFT). We note here that the silicon vacancy in its neutral state has been experimentally verified in 3C-SiC [14], but has received no attention in the theoretical literature. In 3C-SiC only the  $V_{\text{Si}}^{-1}$  defect has been addressed [15, 16]. The  $V_{\text{Si}}$  center, in its neutral charge configuration, can be modeled as a spin-1 defect that evolves in the magnetic environment constituted by the spin-1/2 nuclear spin bath around it.

Highly transition-selective microwave control pulses [5] can be used to effectively reduce the three electron spin’s eigenstates to two in the resulting dynamics, so that it can be considered as a qubit.

The nuclear spin bath induces noise at low frequencies for the point defect. This is typically the case in Nuclear Magnetic Resonance (NMR), where the interesting experimental signal is generated by nonequilibrium electron spin magnetization (equivalent to its coherence) precessing about an external magnetic field [17]. Due to the spatial field inhomogeneity, the measured signal in a Free-Induction Decay (FID) process is defocused and displays a characteristic non-exponential decay resulting in inhomogeneous broadening of the spectral lines. Analogous effects occur in solid-state implementations of qubits and originate from time-inhomogeneities due to repetitions of measurement protocols [18, 19, 20]. One way of refocusing can be achieved by the Hahn-echo sequence, an established technique applied recently to investigate the residual decoherence of divacancy defects in 4H-SiC in ref. [9]. Here we consider both the FID and Hahn-echo sequences applied to the considered defect employing the Cluster Correlation Expansion (CCE) theory [21]. This method consists in breaking up the bath in uncorrelated clusters containing different numbers of interacting nuclear spins, and thereby expressing the qubit coherence as a product of all the contributions coming from the different clusters.

The rest of the paper is organized as follows: in section 2 we describe the model and the methodology behind the *ab initio* calculation for the energetics of the neutral and charged silicon vacancies in 3C-SiC, as well as the calculation of the magnetic parameters of the system plus environment Hamiltonian. Section 3 discusses the analysis of the  $V_{Si}$  formation energy, in its different charge states, as a function of the Fermi level. In section 4 we present our results on the *ab initio* calculation of the hyperfine tensor components, describing the interaction between the  $V_{Si}$  and the nuclear spins in the first two neighbor shells, and the calculation of the Zero-Field Splitting (ZFS) tensor components. In section 5, based on the system’s parameters derived via *ab initio* methods, we calculate both analytically and numerically the spin coherence after free evolution (FID) and under the Hahn-echo sequence, at first and second order of the CCE expansion. In the process, we derive estimates of the decoherence time. Finally, in section 6 our conclusions and ideas for further work are discussed.

## 2 Model and methodology

*Ab initio* methods based on DFT are important to calculate, among others, the structural, electronic, optical and magnetic properties of molecules and solids [22].

They may be used also to calibrate EPR Hamiltonians associated to electron spins interacting with nuclear spin baths, allowing to calculate, for instance, the hyperfine tensor components [23] and the ZFS tensor components [24]. Our system's Hamiltonian can be written as [4]

$$\mathcal{H} = \mathcal{H}_e + \sum_i \mathbf{S} \cdot \mathbf{A}_i \cdot \mathbf{I}_i - \sum_i \mu_n \mathbf{B} \cdot \mathbf{g}_i \cdot \mathbf{I}_i + \sum_{i < j} \mathbf{I}_i \cdot \mathbf{B}_{ij} \cdot \mathbf{I}_j, \quad (2.1)$$

$$\mathcal{H}_e = D \left[ S_z^2 - \frac{1}{3} S(S+1) \right] + E (S_x^2 - S_y^2) - \mu_e \mathbf{B} \cdot \mathbf{g}_e \cdot \mathbf{S}. \quad (2.2)$$

The first term in Eq. 2.1 is the electron spin Hamiltonian, which is composed by the ZFS terms (first and second term of Eq. 2.2), describing the electron spin's self-interaction, and the Zeeman interaction with an external applied magnetic field (last term of Eq. 2.2). The last three terms of Eq. 2.1 (where  $i, j = 1, \dots, N$  indicate the nuclear spin and  $\mu_n$  is the nuclear magneton) are the magnetic hyperfine interactions between the electron spin and the Si<sup>29</sup> and C<sup>13</sup> nuclear spins, the Zeeman terms for each nuclear spin and the dipolar interactions between nuclear spins, respectively. From now on, the pure-dephasing approximation [25, 26] is performed on Eq. 2.1, so that no transition of the electron spin takes place by exchanging energy with the environment. Our working Hamiltonian is (the choice of putting  $E = 0$  is justified in Appendix A) [26]

$$\mathcal{H} = DS_z^2 + \gamma_e B_z S_z + \sum_{i=1}^N \gamma_i B_z I_{iz} + S_z \otimes \sum_{i=1}^N (A_i I_{iz} + B_i I_{ix}) + \mathcal{H}_{n-n}, \quad (2.3)$$

where  $\mathcal{H}_{n-n}$  is the last term of Eq. 2.1,  $A_i \equiv A_{zz}^i$  and  $B_i \equiv \sqrt{A_{zx}^i{}^2 + A_{zy}^i{}^2}$ , whereas  $A_{zx}$ ,  $A_{zy}$  and  $A_{zz}$  are the elements of the third row of the hyperfine tensor. Note that Hamiltonian 2.3 commutes with the electron spin  $S_z$  operator, so that it can be expressed in the spin operator eigenbasis  $\{|1\rangle, |0\rangle, |-1\rangle\}$ , giving rise to [9]

$$\mathcal{H} = \sum_{m_S=1,0,-1} |m_S\rangle \langle m_S| \otimes \mathcal{H}_{m_S}, \quad (2.4)$$

where

$$\mathcal{H}_{m_S} = \omega_{m_S} + \mathcal{H}_B + m_S \sum_{i=1}^N (A_i I_{iz} + B_i I_{ix}). \quad (2.5)$$

Furthermore,  $\mathcal{H}_B = \sum_{i=1}^N \gamma_i B_z I_{iz} + \mathcal{H}_{n-n}$  is the bath Hamiltonian. Finally,

$$\omega_1 = D + \omega_e, \quad (2.6)$$

$$\omega_0 = 0, \quad (2.7)$$

$$\omega_{-1} = D - \omega_e, \quad (2.8)$$

where  $\omega_e = \gamma_e B$  is the Larmor frequency of the electron spin, are the eigenvalues of the electron spin Hamiltonian  $\mathcal{H}_e$  (first and second term of Eq. 2.3). A direct consequence of the form of Hamiltonian 2.4 is that, by opportunely initializing the electron spin (more on that in section 5) and appropriately choosing the control pulses as having precisely the right frequency  $\omega_1$ , the  $|-1\rangle$  state can be frozen out of the dynamics since no transitions are allowed towards it. Therefore, the electron spin effectively behaves as a qubit [9], and we will call it qubit from this point forward.

In this context, *ab initio* methods are used to capture physical effects due to the 3D distribution of the defect's spin density, which mainly extends until the third neighbor shell in 3C-SiC crystal structure (see Fig. 1a). These effects are not included in the semiclassical approximation, where the electron and nuclear spins are considered as classical magnetic point-dipoles interacting with each other. In the semiclassical approximation, the hyperfine tensor can be written as

$$\mathcal{A}_i = \frac{\mu_0 \gamma_i \gamma_e}{4\pi r_i^3} \left( 1 - \frac{3\mathbf{r}_i \mathbf{r}_i}{r_i^2} \right), \quad (2.9)$$

where  $\mu_0$  is the vacuum magnetic permeability,  $\gamma_i$  and  $\gamma_e$  are the  $i$ -th nuclear spin and electron spin gyromagnetic ratios, respectively, whereas  $\mathbf{r}_i$  is the position vector of the  $i$ -th nuclear spin with respect to the qubit, its modulus  $r_i$  being the distance between the two. Of course, as noticed, Eq. 2.9 is no longer applicable in the immediate vicinity of the qubit.

For our computational study we have used the density functional theory as implemented in the open-source Quantum Espresso (QE) code [12] for the calculation of the energetic and magnetic properties of the  $V_{Si}$  in 3C-SiC. We considered a  $7 \times 7 \times 7$  3C-SiC supercell starting from a primitive fcc unit cell, containing 686 atoms, for the calculation of the formation energy [27], whereas a  $6 \times 6 \times 6$  supercell, containing 432 atoms, was employed for the evaluation of the EPR-related parameters like the hyperfine and ZFS tensor components. We used the Perdew-Burke-Ezernhof implementation [28] of the generalized gradient approximation for the description of the exchange-correlation functional. Ultrasoft pseudopotentials [29] were used for standard ground-state properties, whereas hyperfine interactions and ZFS tensors were computed with norm-conserving pseudopotentials [30], as the latter showed a better agreement with respective experimental results [15]. The formation energy was evaluated for the  $V_{Si}$  in various charged configurations considering a non-collinear scheme for the magnetization. EPR calculations were instead performed by using a collinear magnetization along the [001] lattice direction, in order to better comply with usual experimental setups, where the external magnetic field is applied along the growth direction (which coincides with the [001] crystal direction for most 3C-SiC growths [7]). Convergence was achieved with an

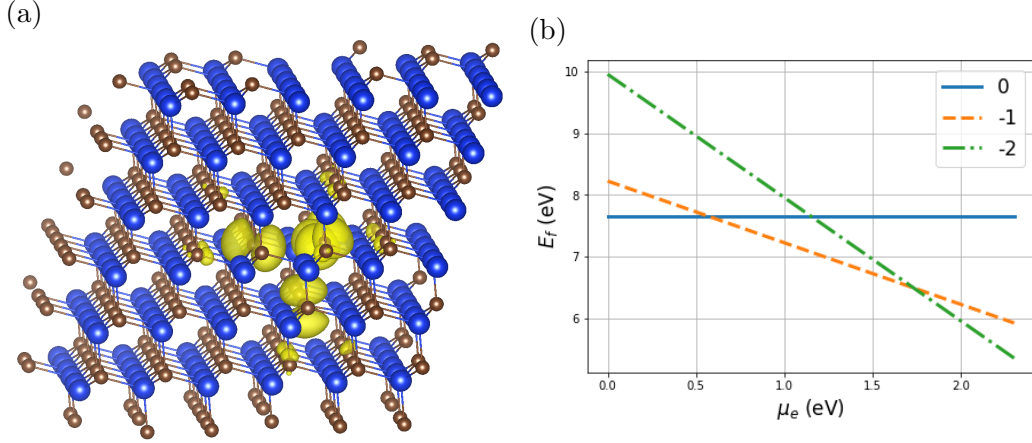


Figure 1: (a) 3D spin density around a neutral  $V_{Si}$  in 3C-SiC. The spin density differences are mainly extended until the third neighbor shell. The wave functions are calculated for a  $6 \times 6 \times 6$  3C-SiC supercell. (b) Formation energies of a neutral, -1 and -2 charged  $V_{Si}$  as a function of the electrochemical potential within the bandgap, for non-collinear calculations in a 686-atom 3C-SiC supercell.

asymmetric  $3 \times 3 \times 3$  k-point grid [31] having an offset with respect to the  $\Gamma$  point. Upon completion of the DFT calculations, the QE wave functions were used as an input in the QE Gauge-Including Projector Augmented-Wave (QE-GIPAW) code [13, 32], to calculate the hyperfine tensor components describing the  $V_{Si}$ -nuclear spins interaction. In addition, they were used to calculate the ZFS tensor components with the aid of the PyZFS code [33]. Finally, in order to better understand if the stacking sequence of the SiC polytype has important implications in the magnetic properties of the defect, hyperfine tensor calculations were also performed for a neutral  $V_{Si}$  in hexagonal 4H-SiC (for both k and h sites).

### 3 Formation energy

An important issue for the determination of the stability of a particular defect under given thermodynamic conditions regards the energetic competition between its various charged states. Here we have calculated the formation energy of the neutral, and charged,  $V_{Si}$  within a 3C-SiC  $7 \times 7 \times 7$  supercell, with a  $3 \times 3 \times 3$  asymmetric k-point grid. The formation energy  $E_f$  of a defect  $X$  can be defined as the energy difference between the investigated system and the components in

their reference states [34], i.e.

$$E_f [X^q] = E_{\text{tot}} [X^q] - E_{\text{tot}} [\text{bulk}] - \sum_i n_i \mu_i + \frac{q}{e} (E_{\text{VBM}} + \mu_e) + E_{\text{corr}}. \quad (3.1)$$

$E_{\text{tot}} [X^q]$  is the total energy of the host crystal with the defect with charge  $q$ , where  $e > 0$  is the elementary charge of the electron,  $E_{\text{tot}} [\text{bulk}]$  is the total energy of the same cell of crystal without the defect, and  $n_i \mu_i$  is the reference energy of added (or subtracted with a change of sign) atoms of element  $i$  at chemical potential  $\mu_i$ . The term in parenthesis accounts for the chemical potential of the electron(s) involved in charging the defect.  $E_{\text{VBM}}$  is the valence band maximum as given by the QE band structure calculation for the bulk material, and  $\mu_e$  is the electron chemical potential defined here with respect to the top of the corresponding valence band. The  $\mu_e$  parameter can then be treated as a free parameter, allowing to account for a shift of the Fermi level, e.g., due to doping. Note that  $\mu_e = E_{\text{gap}}/2$  corresponds to the undoped semiconductor case, where  $E_{\text{gap}}$  is the intrinsic semiconductor band gap. Finally,  $E_{\text{corr}}$  is a sum of relevant correction terms, the most important of which is the monopole correction term, taking into account the electrostatic interaction between the charged defect and its periodic replicas within the *ab initio* simulations. The monopole correction term can be written as [35]

$$E_{\text{corr}} = \frac{q^2 \alpha}{2\epsilon L}, \quad (3.2)$$

where  $q$  is the charge of the defect,  $\alpha$  is the Madelung constant associated to our crystal structure,  $\epsilon$  is the SiC experimental dielectric constant and  $L$  is the distance between the defect and its periodic replicas. For the neutral  $V_{\text{Si}}$  we have calculated  $E_{\text{tot}} [V_{\text{Si}}^0] - E_{\text{tot}} [\text{bulk}]$  and  $\mu_{\text{Si}}$  by using QE, whereas for the charged defects, for which  $q$  is different from zero, we have also calculated the valence band maximum (see Eq. 3.1). Upon structural relaxation inducing a local reconstruction around the defected site [36], the calculated magnetization for the  $V_{\text{Si}}^0$ ,  $V_{\text{Si}}^{-1}$  and  $V_{\text{Si}}^{-2}$  defects was the one expected for a defect with electron spin-1, 3/2 and 1, respectively [37]. Fig. 1a shows the spin density around the central  $V_{\text{Si}}$ , which extends until the third neighbor shell. This nonzero spin density is modeled and implemented in the QE-GIPAW code and allows us to go beyond the semiclassical magnetic point-dipole approximation of Eq. 2.9 (see the next section).

As we can see in Fig. 1b, in which the formation energy of a  $V_{\text{Si}}$  with different charge states is shown as a function of the Fermi level with respect to the valence band maximum (corrected with the monopole correction term given in Eq. 3.2), our *ab initio* results demonstrate the stability of the neutral state for *p*-doped 3C-SiC samples. These results are in good agreement with previous studies [27, 36, 35] and along with the experimental verification of the defect in its

atom	$A_{xx}$	$A_{yy}$	$A_{zz}$
C <sub>1</sub>	26.2	26.2	84.5
C <sub>2</sub>	27.4	27.4	85.6
C <sub>3</sub>	28.8	28.8	87.1
C <sub>4</sub>	27.5	27.5	85.7
Si <sub>1</sub> – Si <sub>12</sub>	7.3	7.6	6.8

Table 1: *Ab-initio* calculated values (in MHz) for the hyperfine tensor components describing the interaction between a neutral  $V_{\text{Si}}$  in 3C-SiC and the nuclear spins in the first and second neighbor shells. The values are obtained by using the QE-GIPAW code [32].

neutral state [14] the theoretical study of its hyperfine interactions is motivated. Another motivation for studying defects that are stable in *p*-doped 3C-SiC samples is the great potential in applications of Al-doped 3C-SiC three gates devices in the MOSFET industry [38]. We note instead that focus has been mainly put to the  $V_{\text{Si}}^{-1}$  charged state in previous reports [15, 16, 39, 14], or to the neutral vacancy only for hexagonal SiC [40]. Within this context, in the next section the hyperfine interactions for a  $V_{\text{Si}}^0$  in 4H- and 3C-SiC are calculated by means of the DFT. Moreover, the ZFS tensor components of a  $V_{\text{Si}}^0$  in 3C-SiC are calculated as well.

## 4 Hyperfine interactions and Zero Field splitting

The results of our *ab initio* calculations can be used to define the hyperfine and ZFS tensors from first principles with the aid of the QE-GIPAW and PyZFS codes, respectively. Table 1 shows the hyperfine tensor components describing the interaction between a neutral  $V_{\text{Si}}$  in 3C-SiC and the nuclear spins in the first and second neighbor shells. In Tables 2 and 3, we show the same components for a neutral  $V_{\text{Si}}$  in 4H-SiC, located in the two nonequivalent 4H sites (i.e., *k* and *h*), respectively. It is important to notice the different crystal structures (cubic and hexagonal) and basal plane orientations ([001] for 3C-SiC and [0001] for 4H-SiC) of the two SiC polytypes, which have an impact on the values obtained for the hyperfine interactions. For example, the 4H-SiC polytype shows hyperfine tensor components for one of the first neighbor C<sup>13</sup> nuclei (i.e., the one corresponding to the [0001]-axis of the hexagonal cell, or C<sub>3</sub> for the *k* site and C<sub>2</sub> for the *h* site) that have different values with respect to the other components. This is due to the parallel collinear magnetization along the [0001] direction imposed in the DFT calculations, along



atom	$A_{xx}$	$A_{yy}$	$A_{zz}$
C <sub>1</sub>	24.5	24.4	76.3
C <sub>2</sub>	24.5	24.4	76.2
C <sub>3</sub>	34.4	34.4	110.4
C <sub>4</sub>	24.5	24.4	76.2
Si <sub>1</sub> – Si <sub>12</sub>	7.5	7.8	6.9

Table 2: *Ab-initio* calculated values (in MHz) for the hyperfine tensor components describing the interaction between a neutral  $V_{\text{Si}}$  (k site) in 4H-SiC and the nuclear spins in the first and second neighbor shells. The values are obtained by using the QE-GIPAW code [32].

atom	$A_{xx}$	$A_{yy}$	$A_{zz}$
C <sub>1</sub>	24.3	24.2	75.1
C <sub>2</sub>	34.2	34.2	112.3
C <sub>3</sub>	24.4	24.3	76.0
C <sub>4</sub>	24.7	24.6	77.1
Si <sub>1</sub> – Si <sub>12</sub>	7.5	7.8	6.9

Table 3: *Ab-initio* calculated values (in MHz) for the hyperfine tensor components describing the interaction between a neutral  $V_{\text{Si}}$  (h site) in 4H-SiC and the nuclear spins in the first and second neighbor shells. The values are obtained by using the QE-GIPAW code [32].

with the nonequivalent position of the vacancy sites in 4H-SiC. In 3C-SiC, the same behavior is not present due to the equivalent position (same distance from the defect) occupied by each  $\text{C}^{13}$  nucleus in the first neighbor shell, forming a tetrahedron around the central  $V_{\text{Si}}$ . Moreover, the z-axis along which the external magnetic field is applied, coincides with the [001] direction, not with the [111] one (which is the equivalent of the [0001] direction in the cubic polytype). Instead, the surrounding of each  $\text{Si}^{29}$  nucleus in the second neighbor shell is approximately invariant in the three cases, giving rise to similar hyperfine tensor components for the two crystal sites in 4H-SiC and for both polytypes. Note that our results in Tables 2 and 3 are in good agreement with the results of reference [15], whereas the calibration in Table 1 is missing in the literature.

Concerning the ZFS tensor components of the electron spin associated to a  $V_{\text{Si}}$  in 3C-SiC, the values obtained for the axial and transversal components are  $D = 1.68$  MHz and  $E = -0.41$  MHz, respectively. In Appendix A we demonstrate that with our choice of parameters, the presence of both components ( $D$  and  $E$ )

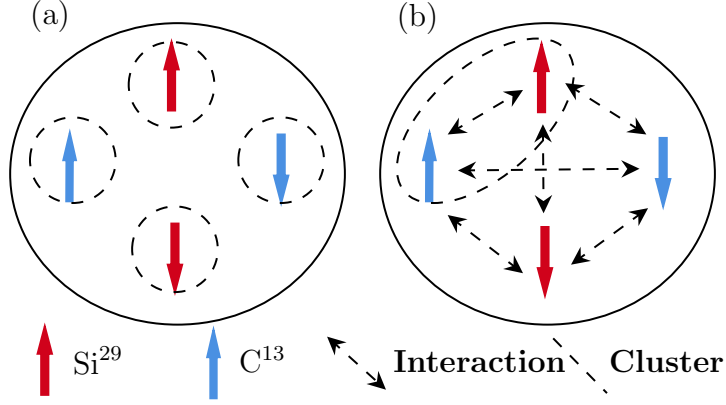


Figure 2: Functioning scheme of the CCE theory, for a generic bath in 3C-SiC containing two  $\text{Si}^{29}$  nuclear spins (in red) and two  $\text{C}^{13}$  nuclear spins (in blue). The spins are in general all interacting with each other via the last term of Eq. 2.1 and are represented in the up or down states with respect to the magnetic field axis. (a): CCE1 approximation in which clusters contain a single nuclear spin. (b): CCE2 approximation containing also two-dimensional clusters (for simplicity only one is shown).

leads to similar results for the electron spin dynamics as when  $E = 0$ . Therefore, in the rest of the paper we will consider  $E = 0$  for simplicity.

## 5 CCE theory

In order to tackle the electron-nuclear spin bath problem we applied the CCE theory. Such theory allows to calculate the off-diagonal component of a solid-state qubit's density matrix in the qubit eigenbasis, also known as coherence, which is our objective. CCE theory has been developed in reference [21] and is perfectly suited for qubits having random interactions with a finite-size bath. As a matter of fact, for small baths the qubit may not finish decohering within the bath spin flip-flop time and higher-order cluster correlations (cfr. Fig. 2) could grow significant. In this case, among the various theories developed such as the density matrix Cluster Expansion (CE) [41], the pair-correlation approximation [42] and the Linked-Cluster Expansion (LCE) [43], only the CCE converges to the exact coherent dynamics of clusters containing multiple spins. In particular, a cluster in this context is defined as a group of fully interacting nuclear spins. CCE theory owes its high convergence property to the fact that it is a bridge between the LCE

and CE approaches. It does not require the need to count or evaluate Feynman diagrams, while being free from the large-bath restriction of the CE. However, typically CCE theory does not converge whenever its  $N$ -th truncation, or CCEN (see below), is not sufficient to model the dynamics. In this case a small term in the recursive expansion in the denominator of Eq. 5.5 below is not balanced by a similar next-order term in the numerator and the final result blows up, thus lying outside of the expected range. The coherent dynamics of finite clusters of bath spins is of special interest in systems with random qubit-bath couplings. Interesting examples are nitrogen-vacancy (NV) centers in diamond and  $V_{\text{Si}}$  in SiC, which are magnetically coupled to randomly located nuclear spins in the vicinity. For such systems, the analysis in reference [42] taking into account only pair-correlations is not sufficient, e.g., to describe free evolution, which is governed by singular interactions between the qubit and the nuclear spins. CCE theory has the advantage of being in principle exact (see below), while simultaneously being of great practical utility as an approximation scheme whenever many-body correlations within the bath are not relevant *and* being more flexible than pair-correlation approaches when higher-order correlations are needed.

In general, the qubit coherence is defined as [9]

$$\mathcal{L}(t) \equiv \frac{\text{tr} \{ \rho_{\text{tot}}(t) S_+ \}}{\text{tr} \{ \rho_{\text{tot}}(0) S_+ \}}, \quad (5.1)$$

where  $\rho_{\text{tot}}(t)$  is the total qubit plus bath density operator at time  $t$ ,  $S_+ = S_x + iS_y$  is the qubit raising operator and  $\rho_{\text{tot}}(0) = \rho_{\text{S}}(0) \otimes \rho_{\text{B}}(0)$  is the initial state of the overall system. In the dipolar approximation of Eq. 2.3 the qubit eigenbasis coincides with a subset of the  $S_z$  spin operator eigenbasis, i.e.  $\{|1\rangle, |0\rangle\}$ . The qubit is prepared in the pure state  $\rho_{\text{S}}(0) = |\Psi\rangle\langle\Psi|$ , where

$$|\Psi\rangle = \frac{1}{\sqrt{2}}(|1\rangle + i|0\rangle), \quad (5.2)$$

so that  $\langle S_y \rangle(0) = 1$  and  $\langle S_x \rangle(0) = 0$ . The preparation in state 5.2, together with the chosen form for the control pulses (see below) and the pure-dephasing approximation in Hamiltonian 2.3, ensures that the  $|-1\rangle$  state stays out of the dynamics. The coherence  $\mathcal{L}(t)$  is a complex function having the expectation values of the qubit  $S_x$  and  $S_y$  operators as real and imaginary parts, respectively. Furthermore, Eq. 5.1 becomes intractable rather quickly as the number of nuclear spins in the bath increases. The objective of CCE theory is then to provide a reasonable and computationally achievable approximated version of the whole coherence given in Eq. 5.1. In order to do so, the first step is the implementation of a numerical procedure generating a random bath of nuclear spins. The  $\text{Si}^{29}$  and  $\text{C}^{13}$  nuclear spins are thereby randomly put in our simulated 3C-SiC lattice, by using a random

number generator, according to their natural abundance of 4.7 and 1.1%, respectively. In typical EPR experiments the temperature of the examined sample is  $\sim 10$  K [9, 44], allowing us to consider completely randomized baths in our CCE code, whose collective state at  $t = 0$  can be written as the mixed state

$$\rho_B(0) = \bigotimes_{i=1}^N \frac{I_i}{2}, \quad (5.3)$$

where  $I_i$  is the  $i$ -th nuclear spin identity operator. Furthermore, in order to obtain a correct statistical sampling of the random bath-generating procedure, we calculate the qubit coherence as an average of the coherences associated to  $\mathcal{N}$  different random baths, or  $\mathcal{N}$  different realizations of the numerical procedure. Hence, in calculating the qubit coherence we confirmed that the converged value [9] for  $\mathcal{N}$  in our simulations is  $\mathcal{N} = 50$  (see Appendix A). In the generation of the random baths, other numerical parameters whose convergence is necessary are the radius of the spherical bath,  $R_{\text{bath}}$ , and the distance between nuclear spins beyond which they are no longer interacting, or nuclear spin connectivity,  $r_{\text{dipole}}$ . The converged values for these parameters (see Appendix A) are found to be  $R_{\text{bath}} = 5$  nm and  $r_{\text{dipole}} = 0.8$  nm, as in reference [9].

Once all of this is taken care of, a Python 3 code developed and benchmarked by us, implementing the CCE theory [45], has been used to calculate the dynamics under the FID and the Hahn-echo processes. The CCE equations are the following:

$$\rho_C(t) = U_C \rho_C(0) U_C^\dagger, \quad (5.4)$$

$$\tilde{\mathcal{L}}_{\{C\}} = \frac{\mathcal{L}_{\{C\}}(t)}{\prod_{C'} \tilde{\mathcal{L}}_{\{C'CC\}}}, \quad (5.5)$$

$$\mathcal{L}(t) = \tilde{\mathcal{L}}_{\{0\}} \prod_i \tilde{\mathcal{L}}_{\{i\}} \prod_{i,j} \tilde{\mathcal{L}}_{\{ij\}} \cdots. \quad (5.6)$$

Eq. 5.4 describes the dynamics of the density operator associated to the qubit interacting with a generic cluster  $C$ , while the Hamiltonian in the time evolution operator  $U_C$  is given by Eq. 2.3, where the only nuclear spins within cluster  $C$  are present. Eq. 5.4 is then substituted in Eq. 5.5 through  $\mathcal{L}_{\{C\}}(t)$ , which can be written as

$$\mathcal{L}_{\{C\}}(t) = \frac{\text{tr} \{ \rho_C(t) S_+ \}}{\text{tr} \{ \rho_C(0) S_+ \}}. \quad (5.7)$$

Eq. 5.5 is the definition of the contribution to the coherence coming from cluster  $C$ . Finally, the coherence in Eq. 5.6 is calculated as the product of all the contributions coming from the different uncorrelated clusters. Therefore, since the expansion of Eq. 5.6 can be cut from a given cluster dimension onward, the order

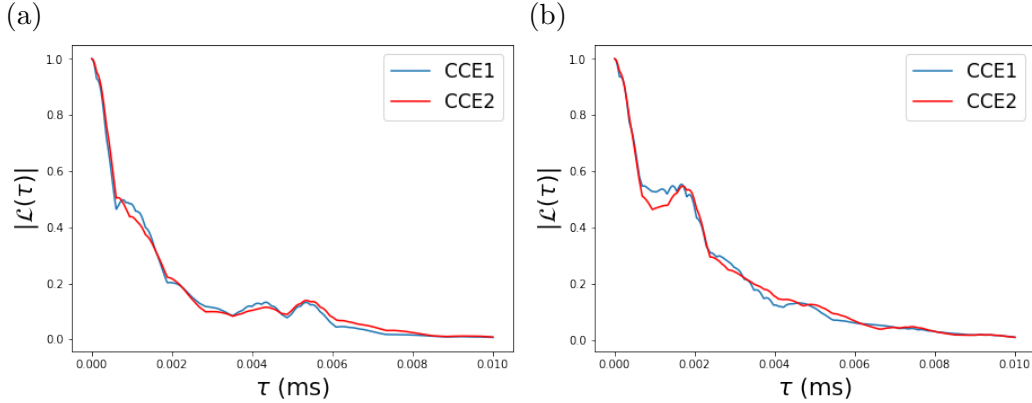


Figure 3: FID evaluated with CCE1 and CCE2 with semiclassical hyperfine tensor components: absolute value of the coherence of a neutral  $V_{\text{Si}}$  in 3C-SiC as a function of free evolution time. The external magnetic field is 200 G (a) and 500 G (b). The curves are averaged over 50 different baths.

of approximation of the theory is defined as the number of nuclear spins inside the biggest clusters we include in Eq. 5.6. Consequently,  $\text{CCE}N$  is the implementation of CCE theory where the biggest clusters we consider contain  $N$  different nuclear spins. In the remainder of the paper we focus exclusively on the CCE1 and CCE2 approaches, with clusters containing single and interacting pairs of nuclear spins, respectively (see Fig. 2 for the functioning scheme of the CCE1 and CCE2 approaches). The benchmark was done against Seo et al. [9], whose study is focused on a divacancy in 4H-SiC.

## 5.1 Free Induction Decay

The research on FID is interesting for many reasons. In the literature experiments are described that elucidate the quantum mechanical origins of the FID signal and spin noise [46]. FID has also been used as a means of controlling the phase and amplitude of extreme ultraviolet photons [47]. Our main objective in studying FID, and the goal of this subsection, is to evaluate the qubit’s decoherence time after free evolution and to compare it with the one we obtain after a given control procedure is applied (cfr. subsection 5.2).

Therefore, in this subsection we focus on the FID process [44], i.e. we let the system freely evolve after the preparation of the qubit. The preparation is obtained via the application of a  $\pi/2$  pulse to the qubit in the  $|0\rangle$  state, so that the initial state is the one given in Eq. 5.2, and the entire FID process can be

described as

$$\rho_{\text{FID}}(\tau) = U_{\text{FID}}(\tau)\rho_{\text{S}}(0)U_{\text{FID}}^\dagger(\tau), \quad (5.8)$$

where  $U_{\text{FID}}(\tau) = e^{-i\mathcal{H}\tau}e^{-i\pi/2S_x}$  is the FID propagator,  $\rho_{\text{S}}(0) = |0\rangle\langle 0|$  and the system's Hamiltonian is the pure-dephasing one given by Eq. 2.3. The real and imaginary parts of the coherence can be analytically calculated in the pure-dephasing approximation and CCE1 case, i.e. whenever we can write the Hamiltonian in the form of Eq. 2.4 and safely neglect the  $\mathcal{H}_{n-n}$  interaction between nuclear spins inside the bath Hamiltonian in 2.5. Then we substitute Eq. 2.4 in Eq. 5.1 through  $\rho_{\text{tot}}(t)$ , and the analytical expressions we obtain are the following [44],

$$\langle S_x \rangle_{\text{FID}}(\tau) = -\sin[(\omega_1 - \omega_0)\tau] f_{\text{B}}(\tau), \quad (5.9)$$

$$\langle S_y \rangle_{\text{FID}}(\tau) = \cos[(\omega_1 - \omega_0)\tau] f_{\text{B}}(\tau), \quad (5.10)$$

where

$$f_{\text{B}}(\tau) = \prod_{i=1}^N \left[ \cos\left(\frac{\omega_{I_i}\tau}{2}\right) \cos\left(\frac{\Omega_{I_i}\tau}{2}\right) + \sin\left(\frac{\omega_{I_i}\tau}{2}\right) \sin\left(\frac{\Omega_{I_i}\tau}{2}\right) \frac{\omega_{I_i} + A_i}{\Omega_{I_i}} \right] \quad (5.11)$$

is a factor depending on the nuclear spins, and

$$\Omega_{I_i} = \sqrt{(\omega_{I_i} + A_i)^2 + B_i^2}. \quad (5.12)$$

In Eq. 5.11,

$$\omega_{I_i} = \gamma_i B \quad (5.13)$$

is the Larmor frequency of the  $i$ -th nuclear spin, where  $B$  is the external magnetic field.

Our results on FID, obtained with our customized code, are displayed in Figs. 3 and 4. In Fig. 3 we show a comparison between the absolute value of the qubit's coherence at the CCE1 and CCE2 levels of the theory, for two different external magnetic fields. The CCE1 curves exactly coincide with the analytical ones obtained as a graph of Eqs. 5.9 and 5.10. Note that there is no interesting effect that is modeled in the passage from CCE1 to CCE2, and the two versions give pretty close results. In Fig. 4 we present the same curves at the CCE2 level, both with semiclassical and *ab initio* hyperfine tensor components, for different external magnetic fields. As can be seen, the presence of even one single nuclear spin in the first shells of next-neighbors causes an appreciable change in the coherence, due to the difference in the hyperfine tensor components and therefore in  $\Omega_{I_i}$  (remember that FID can be well-modeled already at CCE1, see Fig. 3).

In order to better understand our FID results and directly correlate differences in the position of the nuclear spins to the modification of the coherence

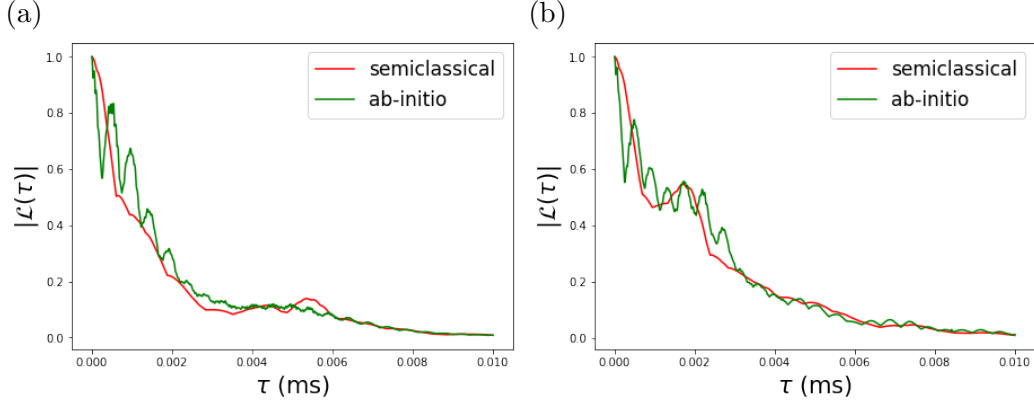


Figure 4: FID evaluated with CCE2 with semiclassical and *ab initio* hyperfine tensor components: absolute value of the coherence of a neutral  $V_{Si}$  in 3C-SiC as a function of free evolution time. The external magnetic field is 200 G (a) and 500 G (b). The curves are averaged over 50 different baths.

modulation frequencies, we propose a manipulation of Eqs. 5.9 and 5.10. In particular, by opportunely rewriting those equations we are able to explicitly obtain the coherence modulation frequencies. To do that we have to express the product of  $N$  terms in Eq. 5.11 as a sum of sinusoidal functions, by repeatedly applying the appropriate trigonometric formulas, so that the modulation frequencies are easily calculated via a Fourier transform. The new expressions can be obtained by exploiting induction considerations (see Appendix B) and the imaginary part of the coherence, e.g., is given by

$$\langle S_y \rangle = \cos(\omega_1 \tau) \Sigma_N(\tau), \quad (5.14)$$

where

$$\begin{aligned} \Sigma_N(\tau) = \frac{1}{2^{2N-1}} \left\{ S_{I_1} \cdots S_{I_N} \left[ (+ - + - \dots + -) + \dots + (+ - - + \dots - +) \right] \right. \\ + S_{I_1} \cdots D_{I_N} \left[ (+ - + - \dots + +) + \dots + (+ - - + \dots - -) \right] + \dots \\ + S_{I_1} \cdots D_{I_i} \cdots D_{I_N} \left[ (+ - \dots + + \dots + +) + \dots + (+ - \dots - \dots - -) \right] \\ \left. + \dots + D_{I_1} \cdots D_{I_N} \left[ (+ + + + \dots + +) + \dots + (+ + - - \dots - -) \right] \right\}. \end{aligned} \quad (5.15)$$

In Eq. 5.15 we have used the shorthand notation

$$(+ - \dots + -) \equiv \cos \left[ (\omega_{I_1}/2 - \Omega_{I_1}/2 + \dots + \omega_{I_N}/2 - \Omega_{I_N}/2) \tau \right], \quad (5.16)$$

whereas

$$S_{I_i} \equiv 1 + \frac{\omega_{I_i} + A_i}{\Omega_{I_i}}, \quad (5.17)$$

$$D_{I_i} \equiv 1 - \frac{\omega_{I_i} + A_i}{\Omega_{I_i}}. \quad (5.18)$$

Inside the curly brackets there are  $2^N$  terms, each of which is multiplied by a sum of  $2^{N-1}$  cosines inside the square brackets. Therefore, without counting the qubit through its level splitting  $\omega_1$  (in which case the modulation frequencies would be doubled, see Appendix B), the modulation frequencies are  $2^N \times 2^{N-1} = 2^{2N-1}$ . Eq. 5.15 reduces to expected results in simple limiting conditions, i.e.

$$\Sigma_N (A = 0, B = 0) = 1, \quad (5.19)$$

$$\Sigma_N (\tau = 0) = 1. \quad (5.20)$$

Eqs. 5.19 and 5.20, coupled with Eq. 5.14, give us the expected behavior of the coherence imaginary part when the qubit is isolated from the environment and at the beginning of the dynamics, respectively. Additional considerations regarding Eq. 5.15 are reported in Appendix B, in particular the numerical calculation of the modulation frequencies in a simple case. Finally, the modulation frequencies, containing information on how each nuclear spin in the bath affects the qubit during the dynamics, can be derived directly from the pure-dephasing Hamiltonian 2.3, in the CCE1 case or whenever  $\mathcal{H}_{n-n} = 0$ . In particular, they are obtained as linear combinations of our system's eigenenergies, as we demonstrate in Appendix C.

At this point, the difference in the modulation frequencies in going from the semiclassical to the *ab initio* curve in Fig. 4 is explained by considering the dependency of those frequencies, given in Eq. 5.15, on the hyperfine tensor components through  $\Omega_{I_i}$ . In particular, in the case where the bath is composed by a single  $C^{13}$  nucleus in the first neighbor shell, there are only two frequencies in the terms  $(+-)$  and  $(++)$ . The first frequency doubles its value, from 13.1 MHz to 29.4 MHz, by using the *ab initio* calibration.

## 5.2 Hahn-echo

In NMR/EPR systems environmental noise takes the form of magnetic field noise that results from the effect of accumulating disturbances from each nuclear spin-generated magnetic field (such static magnetic field inhomogeneity



causes inhomogeneous broadening of the spectral lines [18]). To limit inhomogeneous broadening, we have applied the Hahn-echo sequence [48], an established control technique [44, 9] allowing to refocus the spin coherence and thus enlarge its decoherence time [49, 9], which is the main goal of this subsection.

In this regard, the most important part of the spin-echo sequence is an intermediate  $\pi$  pulse applied to the qubit which allows to refocus the spin coherence resulting from the effect of static magnetic field inhomogeneities [17]. Consequently, the dynamics can be described in the following way:

$$\rho_{\text{HE}}(\tau) = U_{\text{HE}}(\tau)\rho_{\text{S}}(0)U_{\text{HE}}^\dagger(\tau), \quad (5.21)$$

where  $U_{\text{HE}}(\tau) = e^{-i\mathcal{H}\tau/2}e^{-i\pi S_x}e^{-i\mathcal{H}\tau/2}e^{-i\pi/2S_x}$  is the Hahn-echo propagator and  $\rho_{\text{S}}(0)$  is the same as for the FID case. Now, as a first order approximation, at the CCE1 level we can obtain analytical expressions for the coherence real and imaginary parts in the pure-dephasing approximation [9], as in the FID case. Therefore, the qubit coherence components in 5.1, after the Hahn-echo sequence, can be written as [44]

$$\langle S_x \rangle_{\text{HE}}(\tau) = 0, \quad (5.22)$$

$$\langle S_y \rangle_{\text{HE}}(\tau) = \prod_{i=1}^N \left[ 1 - 2k_{+1,0}^i \sin^2 \left( \Omega_{I_i} \frac{\tau}{4} \right) \sin^2 \left( \omega_{I_i} \frac{\tau}{4} \right) \right], \quad (5.23)$$

where

$$k_{+1,0}^i = \frac{B_i^2}{\Omega_{I_i}^2} \quad (5.24)$$

is the modulation depth parameter of the  $i$ -th nuclear spin between the  $|0\rangle$  and  $|+1\rangle$  qubit states. Eq. 5.23 describes fast oscillations of the qubit coherence, or modulations (see Fig. 5), known in the literature as Electron Spin Echo Envelope Modulation (ESEEM), which are due to single nuclear spin transitions [44]. The real part of the coherence is zero also at  $t = \tau$  because of the refocusing action of the central  $\pi$  pulse.

Our results on the Hahn-echo confirm the ones found in the literature [9], and extend them to a neutral  $V_{\text{Si}}$  in 3C-SiC. In particular, the decay of the coherence is obtained already at the second order of approximation of the CCE theory, or CCE2 level, as shown in Fig. 5a (this does not preclude the possibility of having further effects beyond CCE2). The figure shows the coherence of the qubit under the Hahn-echo sequence, for

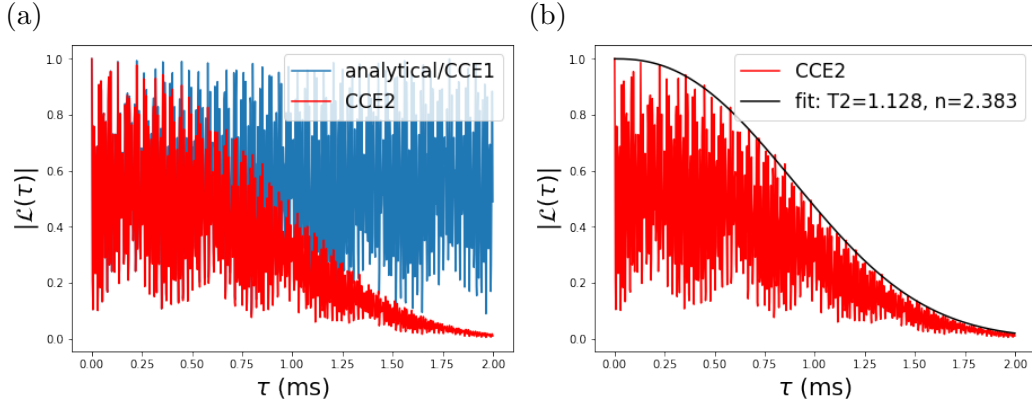


Figure 5: Hahn-echo evaluated with CCE1 and CCE2 with semiclassical hyperfine tensor components: absolute value of the coherence of a neutral  $V_{\text{Si}}$  in 3C-SiC as a function of free evolution time, for an external magnetic field of 200 G. The result is averaged over 50 different baths. (a): the blue curve is the analytical (Eq. 5.23) or CCE1 result and the red one is the CCE2. Notice the coherence decay in the milliseconds range. (b): CCE2 coherence with a fitting exponential function  $e^{-(t/T_2)^n}$  and the optimal values for the parameters  $T_2$ , in ms, and  $n$  in the inset.

an external applied magnetic field of 200 G. The blue curve is the coherence calculated at the first order of approximation of the theory, or CCE1 level, and exactly coincides with the analytical curve obtained as a graph of Eq. 5.23, as in the FID case. This should be the case since Eq. 5.23 is obtained precisely by following the analytical counterpart of the numerical procedure behind the CCE1 approach, i.e. by neglecting  $\mathcal{H}_{n-n}$  in 2.5 and thereby considering the coherence as a product of independent contributions coming from each nuclear spin. Now, as can be seen from Fig. 5, at the CCE2 level (red curve), where also contributions from clusters containing pairs of nuclei are considered, the decay appears (note the difference with FID, for which CCE1 and CCE2 give similar results). Therefore, pairwise interactions within the bath are responsible for a coherence decay that is not cancelled by the echo [9]. Moreover, we observe from Fig. 5b that, under the approximations performed, the predicted coherence decay is in the milliseconds range, whereas for FID is in the 0.01 ms range (this difference is crucial in QT applications). The figure shows the CCE2 coherence and a stretched exponential function fitting its decaying envelope, as well as the optimal val-

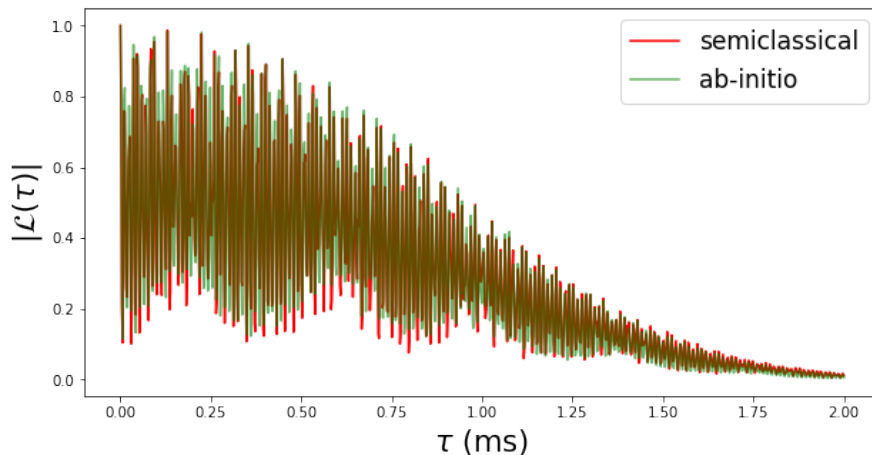


Figure 6: Hahn-echo evaluated with CCE2 with semiclassical (Eq. 2.9) and *ab initio* (Table 1) hyperfine tensor components: absolute value of the coherence of a neutral  $V_{\text{Si}}$  in 3C-SiC as a function of free evolution time, for an external magnetic field of 200 G. The result is averaged over 50 different baths.

ues, obtained via a curve-fitting algorithm, for the Hahn-echo decoherence time  $T_2$  and the stretching factor  $n$  of the exponential. These values are 1.128 ms and 2.383, respectively, for the 200 G curve. Due to the presence of a stretching factor, we demonstrate that also for a  $V_{\text{Si}}$  in 3C-SiC the decay of the coherence envelope is not exponential, which is a typical behavior for qubits in NMR/EPR and in general in the solid state. As a matter of fact, this also happens for superconducting qubits, which are usually subjected to  $1/f$ -type noise from the environment [18].

Then, we have used the *ab initio* calculated values of the hyperfine tensor components listed in Table 1 in our CCE code. The comparison of the resulting coherence curve with the semiclassical one, for an external applied magnetic field of 200 G, is shown in Fig. 6. The main difference is in the modulation effect, whereas the decay, and hence the decoherence time, is almost unchanged. Again, doing the comparison with FID we see that spin-echo protocols are more robust against the hyperfine tensor components change due to the *ab initio* calibration. This is due to the refocusing  $\pi$  pulse that lifts the dependence on one-body interactions, which are more affected by the *ab initio* calibration. This is in turn due to there being

way more one-body interactions where the electron-nuclear spin distance is such that the *ab initio* value is used as opposed to two-body interactions where *both* nuclear spins are close enough to require the *ab initio* calibration. This behavior is understood by looking at Eq. 5.23, for which a similar reasoning used in the passage from Eq. 5.10 to Eq. 5.14 can be applied to analytically calculate the modulation frequencies. Those frequencies depend both on the single nuclear spin Larmor frequencies and the hyperfine tensor components through  $\Omega_{I_i}$ . Therefore, if any of the 50 random baths in a given simulation happens to have a nuclear spin in the first or second neighbor shell, the hyperfine tensor components entering Eq. 5.23, and thereby the modulations of the coherence, will be modified. We find the change of the modulation frequencies by using the *ab initio* calibration to be of the same order of magnitude as in the FID case (see the last paragraph of subsection 5.1). As for the decoherence effect, which is at least caused by two-body interactions between nuclear spins (it appears at least at the CCE2 level), the probability of having two nuclear spins in the first and second neighbor shell is less than the probability of having just one, thus conditioning less the coherence decay. This is a consequence of the chosen numerical random bath-generating procedure.

## 6 Conclusions

In conclusion, we have used the density functional theory to study the formation energy of the silicon vacancy in 3C-SiC, analyzing its charge states and establishing their range of stability as a function of the Fermi level. By doing so, we have demonstrated that the less studied neutral charge state of the  $V_{Si}$  is the most stable one for *p*-doped 3C-SiC samples. Moreover, our results on the hyperfine tensor components show significant deviation with respect to the semiclassical estimates of the model parameters obtained with Eq. 2.9. We have studied both Hahn spin-echo and FID as protocols applied to our qubit, finding the equations (Eqs. 5.9 and 5.10) that describe FID when the nuclear spins are non-interacting with each other. By appropriately rewriting those equations we have been able to analytically calculate, at the CCE1 level, the FID modulation frequencies and directly associate them to the Hamiltonian eigenvalues, and hence to the system's magnetic parameters. Furthermore, by applying the CCE theory by means of our in-house code, we have evaluated within reliable approximations the ESEEM phenomenon and

the decoherence of the spin associated to the defect when Hahn spin-echo protocols, and FID processes, with different magnetic field values are applied to the system. The estimated  $V_{\text{Si}}$  decoherence time in 3C-SiC, after a Hahn-echo protocol has been applied, is in the milliseconds range, thus gaining at least two orders of magnitude with respect to FID. We have also evaluated the non-exponential character of the coherence decay, which is typical for qubits in solid state devices. Finally, we have demonstrated that, for the spin-echo, modeling the 3D distribution of the spin density in the vicinity of the qubit in our CCE simulations, by using *ab initio* methods based on DFT, has an effect on the coherence modulations known as the ESEEM phenomenon, but not as much on the decoherence effect, which is important for QT applications. For the FID process the effect is instead more pronounced. This is due to the FID process being dominated by one-body interactions between the qubit and the nuclear spins in the bath, and to these interactions being more affected by the *ab initio* calibration than the two-body ones between nuclear spins.

We hope that our work can inspire new studies on the cubic polytype of SiC, which is gaining new attention within the scientific literature.

This work was partially funded by the Italian Ministry for Education, University and Research (MIUR) in the framework of the National Project PON EleGaNTe (Electronics on GaN-based Technologies), Grant No. ARS01\_01007. T.F. acknowledges a fruitful conversation and exchange of emails with Mykyta Onizhuk from the group of Giulia Galli.

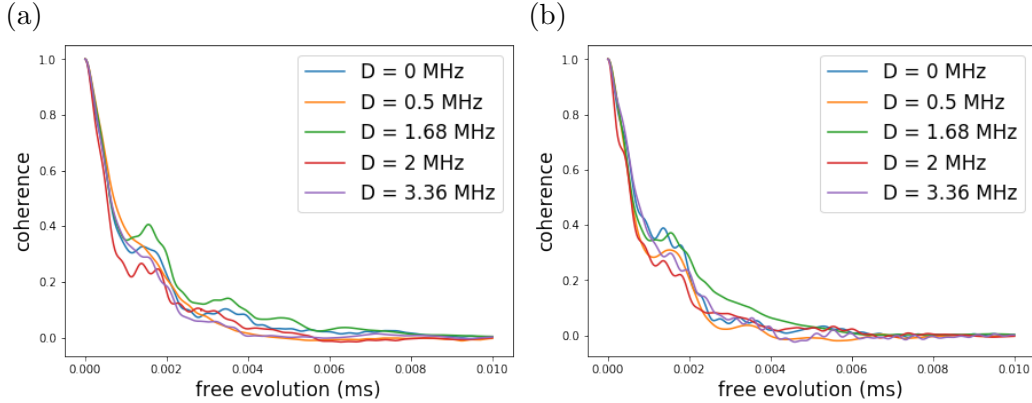


Figure A.1: CCE2 absolute value of the coherence of a neutral  $V_{\text{Si}}$  in 3C-SiC as a function of free evolution time, with different values for the axial component  $D$  of the ZFS tensor, for an external magnetic field of 500 G. The dynamics implemented is a free evolution, or FID process, and the results are averaged over 50 different baths. (a): the transversal component  $E$  of the ZFS tensor is absent. (b): the transversal component  $E$  of the ZFS tensor is present ( $E = -0.41$  MHz). The curves are obtained with the PyCCE code from the Galli group [50].

## A Supplemental material on the simulations

In this Appendix we are going to present all the results on the convergence of the parameters entering our simulations.

First of all, in Fig. A.1 we show the dependence of the coherence on the axial component  $D$  in a FID process. Since in our CCE code the Hamiltonian is written in the pure-dephasing approximation from the start, these results are obtained by using the PyCCE code from the Galli group [50]. As can be seen from the figure, by adding  $E = -0.41$  MHz (right panel) the result does not change appreciably, so that our choice of neglecting  $E$  is justified. Then, in Fig. A.2 we have studied the dependence of the coherence on the radius of the spherical bath  $R_{\text{bath}}$  at the CCE1 level, which is sufficient for analyzing FID.

From the figure we see that already for a bath with a radius of dimension  $R_{\text{bath}} = 2.5$  nm the result is almost completely converged, justifying our choice of  $R_{\text{bath}} = 5$  nm.

Finally, in Fig. A.3 we show the dependence of the coherence on the

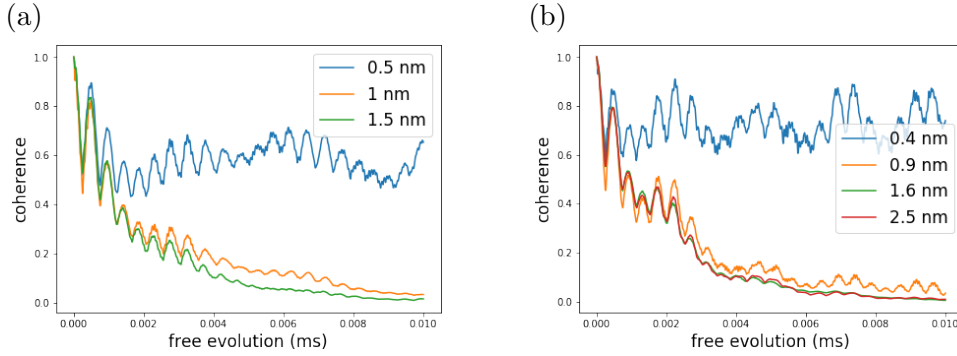


Figure A.2: CCE1 absolute value of the coherence of a neutral  $V_{Si}$  in 3C-SiC as a function of free evolution time, with different values for the radius of the spherical bath  $R_{bath}$ , for an external magnetic field of 340 G (a) and 500 G (b). The dynamics implemented is a free evolution, or FID process, and the results are averaged over 50 different baths.

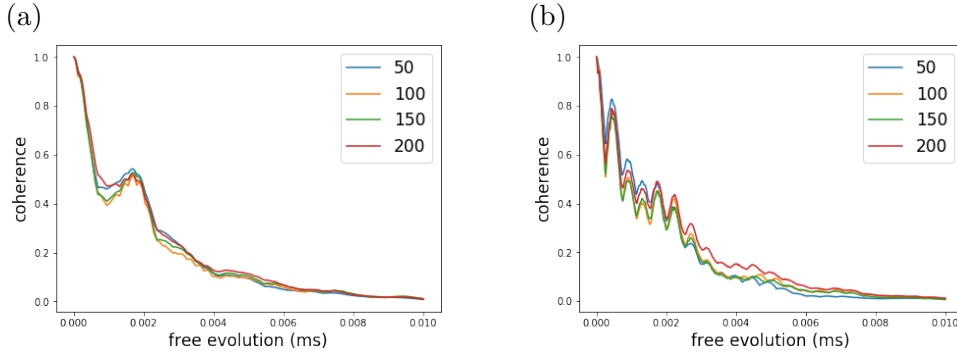


Figure A.3: CCE1 absolute value of the coherence of a neutral  $V_{Si}$  in 3C-SiC as a function of free evolution time, with different values for the number of bath realizations  $\mathcal{N}$ , for an external magnetic field of 500 G. The dynamics implemented is a free evolution, or FID process, and the radius of the spherical bath is  $R_{bath} = 4$  nm. (a): the hyperfine tensor components are calculated via Eq. 2.9. (b): the hyperfine tensor components are calculated via *ab initio* methods based on DFT (Table 1).

number of realizations of the bath  $\mathcal{N}$ , again at the CCE1 level and for a reduced bath of  $R_{\text{bath}} = 4$  nm. Note that already a mean over 50 different baths is sufficient to obtain a reasonably well-converged coherence curve, which is why we choose  $\mathcal{N} = 50$  in the main body of the paper.



## B Induction considerations

In this appendix we give a non-rigorous derivation of Eq. 5.15 of the main text, starting from Eq. 5.11, by exploiting induction considerations.

Let's start by considering the case where there is a single nuclear spin in our bath, i.e.  $n = 1$ . In this case, by using trigonometric formulas, Eq. 5.11 can be written as

$$\Sigma_1(\tau) = \frac{1}{2} \left( S_{I_1} \cos \left[ \left( \frac{\omega_{I_1}}{2} - \frac{\Omega_{I_1}}{2} \right) \tau \right] + D_{I_1} \cos \left[ \left( \frac{\omega_{I_1}}{2} + \frac{\Omega_{I_1}}{2} \right) \tau \right] \right), \quad (\text{B.1})$$

and thus we have two terms and two modulation frequencies, one for each term. In the case  $n = 2$  we have instead four terms and eight modulation frequencies, two for each term, as can be seen by the following formula:

$$\begin{aligned} \Sigma_2 = \frac{1}{8} \left\{ S_{I_1} S_{I_2} \left[ \cos \left[ \left( \frac{\omega_{I_1}}{2} - \frac{\Omega_{I_1}}{2} + \frac{\omega_{I_2}}{2} - \frac{\Omega_{I_2}}{2} \right) \tau \right] + \cos \left[ \left( \frac{\omega_{I_1}}{2} - \frac{\Omega_{I_1}}{2} - \frac{\omega_{I_2}}{2} + \frac{\Omega_{I_2}}{2} \right) \tau \right] \right] \right. \\ + S_{I_1} D_{I_2} \left[ \cos \left[ \left( \frac{\omega_{I_1}}{2} - \frac{\Omega_{I_1}}{2} + \frac{\omega_{I_2}}{2} + \frac{\Omega_{I_2}}{2} \right) \tau \right] + \cos \left[ \left( \frac{\omega_{I_1}}{2} - \frac{\Omega_{I_1}}{2} - \frac{\omega_{I_2}}{2} - \frac{\Omega_{I_2}}{2} \right) \tau \right] \right] \\ + D_{I_1} S_{I_2} \left[ \cos \left[ \left( \frac{\omega_{I_1}}{2} + \frac{\Omega_{I_1}}{2} + \frac{\omega_{I_2}}{2} - \frac{\Omega_{I_2}}{2} \right) \tau \right] + \cos \left[ \left( \frac{\omega_{I_1}}{2} + \frac{\Omega_{I_1}}{2} - \frac{\omega_{I_2}}{2} + \frac{\Omega_{I_2}}{2} \right) \tau \right] \right] \\ \left. + D_{I_1} D_{I_2} \left[ \cos \left[ \left( \frac{\omega_{I_1}}{2} + \frac{\Omega_{I_1}}{2} + \frac{\omega_{I_2}}{2} + \frac{\Omega_{I_2}}{2} \right) \tau \right] + \cos \left[ \left( \frac{\omega_{I_1}}{2} + \frac{\Omega_{I_1}}{2} - \frac{\omega_{I_2}}{2} - \frac{\Omega_{I_2}}{2} \right) \tau \right] \right] \right\}. \end{aligned} \quad (\text{B.2})$$

By analyzing Eqs. B.1 and B.2 we find some common behaviors that allow us to infer the form of the equation valid in the general  $n = N$  case to be exactly Eq. 5.15. Furthermore, in the general case we have  $2^N$  terms and  $2^{2N-1}$  modulation frequencies,  $2^{N-1}$  for each term. The number of terms and the number of frequencies per term are not random, and can be understood, or counted, as the number of ways in which we can dispose  $N$  elements from a set of 2 elements, where the same element can be repeated at most  $N$  times (they are thus called dispositions with repetitions). For what concerns the number of terms we have to dispose  $N$  elements from the set of values  $\{S_{I_i}, D_{I_i}\}$  they can take, with a maximum of  $N$  possible repetitions. The number of these dispositions is precisely  $2^N$ . Instead, for the number of frequencies per term we have to dispose  $N - 1$  *pairs* of elements (pairs of signs), all but the first one, from the set of values  $\{+, -\}$  they can take, with

a maximum of  $N - 1$  possible repetitions, *fixing* at the same time the first pair to a  $(+-)$  if the term they are multiplied by starts with an  $S$  or to a  $(++)$  if the term they are multiplied by starts with a  $D$ . Since the cosine is an even function, we can make the opposite choice,  $S \rightarrow (-+)$  and  $D \rightarrow (--)$ , but also in this case the rules remain the same and nothing changes, so that it is a matter of taste.

Finally, we give the version of Eq. 5.14 in which also the  $\cos(\omega_1\tau)$  term is put inside of  $\Sigma_N$ , i.e.

$$\begin{aligned}
\langle S_y \rangle = \frac{1}{2^{2N}} & \left\{ S_{I_1} \cdots S_{I_N} \left[ (- + - + \dots - +) + \dots + (- + + - \dots + -) \right. \right. \\
& + (+ - - + \dots - +) + \dots + (+ - + - \dots + -) \left. \right] \\
& + S_{I_1} \cdots D_{I_N} \left[ (- + \dots - + - -) + \dots + (+ - \dots + - - -) \right. \\
& + (- + \dots - + + +) + \dots + (+ - \dots + - + +) \left. \right] + \dots \\
& + S_{I_1} \cdots D_{I_i} \cdots D_{I_N} \left[ (- + \dots - - \dots - -) + \dots + (+ - \dots - - \dots + +) \right. \\
& + (- + \dots + + \dots - -) + \dots + (+ - \dots + + \dots + +) \left. \right] + \dots \\
& + D_{I_1} \cdots D_{I_N} \left[ (- - - - \dots - -) + \dots + (- - + + \dots + +) \right. \\
& \left. \left. + (+ + - - \dots - -) + \dots + (+ + + + \dots + +) \right] \right\}, \tag{B.3}
\end{aligned}$$

where now a new notation is used,

$$(+ - \dots + -) \equiv \cos \left[ (\omega_1 + \omega_{I_1}/2 - \Omega_{I_1}/2 + \dots + \omega_{I_N}/2 - \Omega_{I_N}/2) \tau \right]. \tag{B.4}$$

In this case there are  $2^{2N}$  modulation frequencies, thus their number being doubled in size, as noticed in the main text. Furthermore, each of the final modulation frequencies appearing in Eq. B.3 can be written as a linear combination of the eigenvalues of the pure-dephasing Hamiltonian, given in Eq. 2.3, in the CCE1 case (see Appendix C).

Now, an interesting calculation to perform is the one involving the modulation frequencies, which can be analytically obtained through Eq. 5.15, in a specific case. The Fourier transform of the signal in time, given in Eq.

5.15, is easily obtained and can be written as

$$\begin{aligned}
\tilde{\Sigma}_N(\omega) = \frac{\pi}{2^{2N-1}} & \left\{ S_{I_1} \cdots S_{I_N} \left[ [+ - + - \dots + -] + [- + - + \dots - +] + \dots \right. \right. \\
& + [+ - - + \dots - +] + [- + + - \dots + -] \\
& + S_{I_1} \cdots D_{I_N} \left[ [+ - + - \dots + +] + [- + - + \dots - -] + \dots \right. \\
& + [+ - - + \dots - -] + [- + + - \dots + +] \left. \right] + \dots \\
& + S_{I_1} \cdots D_{I_i} \cdots D_{I_N} \left[ [+ - \dots + + \dots + +] + [- + \dots - - \dots - -] + \dots \right. \\
& + [+ - \dots - - \dots - -] + [- + \dots + + \dots + +] \\
& + \dots + D_{I_1} \cdots D_{I_N} \left[ [+ + + + \dots + +] + [- - - - \dots - -] + \dots \right. \\
& \left. \left. + [+ + - - \dots - -] + [- - + + \dots + +] \right] \right\}, \tag{B.5}
\end{aligned}$$

where now each term inside the curly brackets is multiplied by a sum of Dirac delta functions, and we have introduced the notation

$$[+ - \dots + -] \equiv \delta [\omega + \omega_{I_1}/2 - \Omega_{I_1}/2 + \dots + \omega_{I_N}/2 - \Omega_{I_N}/2]. \tag{B.6}$$

In passing from Eq. 5.15 to Eq. B.5, we have used the known result

$$\mathcal{F}[\cos(\omega_0 t)] = \pi(\delta[\omega + \omega_0] + \delta[\omega - \omega_0]). \tag{B.7}$$

By examining the signal in frequency, given in Eq. B.5, we see that the Fourier transform will display delta-like peaks in correspondence to each modulation frequency inside the arguments of the delta functions. To exemplify this by means of an example, we report in Fig. B.1 the imaginary part of the FID time signal of a  $V_{\text{Si}}^0$  interacting with a single  $\text{Si}^{29}$  nucleus in the second-neighbor shell, for simplicity, and its normalized Fourier transform obtained via a numerical Fast Fourier Transform (FFT) algorithm. Since in this case  $N = 1$ , the modulation frequencies are 4 (see Appendix B) and are quantitatively predicted by Eq. B.3 to be 0.9448 GHz, 0.9576 GHz, 0.9574 GHz and 0.9451 GHz, respectively. The relative amplitude of the central peaks is given by  $(1 - \frac{\omega_I + A}{\Omega_I}) / (1 + \frac{\omega_I + A}{\Omega_I}) = 0.27$  (see Fig. B.1b). Even though Eq. B.3 can be used to find the modulation frequencies displayed in Fig. 4, a graphical depiction of the peaks of the corresponding Fourier

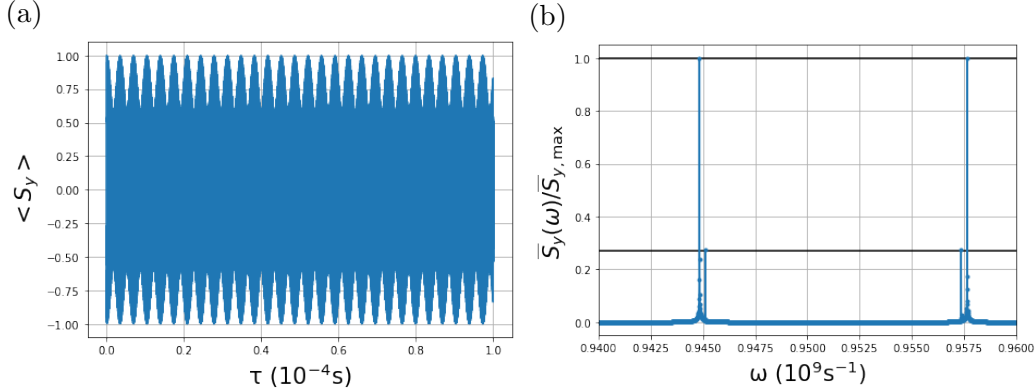


Figure B.1: FID evaluated with CCE1 with *ab initio* hyperfine tensor components: (a) imaginary part of the coherence of a neutral  $V_{\text{Si}}$  in 3C-SiC as a function of free evolution time, for an external magnetic field of 340 G. The bath contains a single  $\text{Si}^{29}$  nucleus in the second-neighbor shell. (b) Normalized Fourier transform of the signal in the time domain obtained via a numerical FFT algorithm.

transform as in Fig. B.1b is impractical due to the presence of  $\sim 2^{3000}$  of them for an entire nuclear spin bath. Furthermore, most of them would not be visible due to the reduced resolution necessary to in principle show all of them in the horizontal axis and the ever-decreasing relative amplitudes of the central peaks. In this sense, the example in Fig. B.1 is extremely useful as a proof of principle of Eq. B.3, in that it shows all the frequencies predicted as peaks in the corresponding Fourier transform in a simple case. Once we have demonstrated the reliability of Eq. B.3, through the example in Fig. B.1 and how we have obtained it in Appendix B, we can proceed towards its application to finding the dominant frequencies of the curves in Fig. 4. We already know that the dominant frequencies, the ones represented by peaks with unitary amplitude in the FFT, are multiplied by the term  $SS \cdots S$  (the first term), since after normalization they are multiplied by 1 and the others by a number between 0 and 1. As we detail in Appendix B, these frequencies are  $2^N$  ( $\sim 2^{1500}$  for a full bath). One of them, the others being very close differing in the second decimal place (see Fig. B.1b), is contained in the term  $(+ - + - \dots + -)$ , i.e.

$$\omega_{\text{dom}} = \omega_1 + \omega_{I_1}/2 - \Omega_{I_1}/2 + \omega_{I_2}/2 - \Omega_{I_2}/2 + \dots + \omega_{I_N}/2 - \Omega_{I_N}/2. \quad (\text{B.8})$$

## C Modulation frequencies

In this Appendix we derive the modulation frequencies from section 5 by following a different approach. Let's start by specializing ourselves to the case in which there is only one nuclear spin in the bath, i.e.  $n = 1$ , and let's write the pure-dephasing Hamiltonian 2.3 in this case,

$$\mathcal{H} = DS_z^2 + \gamma_e B_z S_z + \gamma_1 B_z S_z + AS_z I_z + BS_z I_x. \quad (\text{C.1})$$

The problem's Hilbert space has dimension  $\dim(\mathcal{H}) = 3 \times 2 = 6$ , so that the matrix representing Hamiltonian C.1 is a  $6 \times 6$  one. We report the matrix in the following:

$$\begin{pmatrix} \omega_1 + \frac{\omega_I}{2} + \frac{A}{2} & B/2 & 0 & 0 & 0 & 0 \\ B/2 & \omega_1 - \frac{\omega_I}{2} - \frac{A}{2} & 0 & 0 & 0 & 0 \\ 0 & 0 & \frac{\omega_I}{2} & 0 & 0 & 0 \\ 0 & 0 & 0 & -\frac{\omega_I}{2} & 0 & 0 \\ 0 & 0 & 0 & 0 & \omega_{-1} + \frac{\omega_I}{2} - \frac{A}{2} & -B/2 \\ 0 & 0 & 0 & 0 & -B/2 & \omega_{-1} - \frac{\omega_I}{2} + \frac{A}{2} \end{pmatrix}. \quad (\text{C.2})$$

This is a block-diagonal matrix with three quadrants, one for each of the three electron spin's energy levels. Consequently, the third quadrant is of no interest for us, whereas the second one is already diagonal. It remains to diagonalize the first quadrant to be able to write down the first four eigenvalues, which are given by

$$\omega_1 + \frac{\Omega_I}{2} = E_1, \quad (\text{C.3})$$

$$\omega_1 - \frac{\Omega_I}{2} = E_2, \quad (\text{C.4})$$

$$\frac{\omega_I}{2} = E_3, \quad (\text{C.5})$$

$$-\frac{\omega_I}{2} = E_4, \quad (\text{C.6})$$

where  $\Omega_I$  is defined in Eq. 5.12. Now, from Eq. B.3 we have the  $2^{2N}$ , in this case 4, modulation frequencies, which are the following,

$$\omega_1 - \frac{\omega_I}{2} + \frac{\Omega_I}{2} = E_1 + E_4, \quad (\text{C.7})$$

$$\omega_1 + \frac{\omega_I}{2} - \frac{\Omega_I}{2} = E_2 + E_3, \quad (\text{C.8})$$

$$\omega_1 - \frac{\omega_I}{2} - \frac{\Omega_I}{2} = E_2 + E_4, \quad (\text{C.9})$$

$$\omega_1 + \frac{\omega_I}{2} + \frac{\Omega_I}{2} = E_1 + E_3. \quad (\text{C.10})$$

Eqs. C.7-C.10 are the relations we were looking for between the modulation frequencies and our system's eigenenergies. Furthermore, analogous relations valid in the case  $n = N$  can be easily obtained by using induction considerations.

## References

- [1] Tsunenobu Kimoto and James A Cooper. *Fundamentals of silicon carbide technology: growth, characterization, devices and applications*. John Wiley & Sons, 2014.
- [2] Katsuya Okamura and Ken Takayama. High frequency power supply with 3.3 kv sic-mosfets for accelerator application. In *Materials Science Forum*, volume 897, pages 685–688. Trans Tech Publ, 2017.
- [3] Luciano FS Alves, Ruan CM Gomes, Pierre Lefranc, Raoni de A Pegado, Pierre-Olivier Jeannin, Benedito A Luciano, and Filipe V Rocha. Sic power devices in power electronics: An overview. In *2017 Brazilian Power Electronics Conference (COBEP)*, pages 1–8. IEEE, 2017.
- [4] Stefania Castelletto and Alberto Boretti. Silicon carbide color centers for quantum applications. *Journal of Physics: Photonics*, 2(2):022001, 2020.
- [5] Viktor Ivády, Krisztián Szász, Abram L Falk, Paul V Klimov, David J Christle, Erik Janzén, Igor A Abrikosov, David D Awschalom, and Adam Gali. Theoretical model of dynamic spin polarization of nuclei coupled to paramagnetic point defects in diamond and silicon carbide. *Physical Review B*, 92(11):115206, 2015.
- [6] Debbie G Senesky, Babak Jamshidi, Kan Bun Cheng, and Albert P Pisano. Harsh environment silicon carbide sensors for health and performance monitoring of aerospace systems: A review. *IEEE Sensors Journal*, 9(11):1472–1478, 2009.
- [7] Giuseppe Fiscaro, Corrado Bongiorno, Ioannis Deretzis, Filippo Giannazzo, Francesco La Via, Fabrizio Roccaforte, Marcin Zielinski, Massimo Zimbone, and Antonino La Magna. Genesis and evolution of extended defects: The role of evolving interface instabilities in cubic sic. *Applied Physics Reviews*, 7(2):021402, 2020.
- [8] Francesco La Via, Massimo Zimbone, Corrado Bongiorno, Antonino La Magna, Giuseppe Fiscaro, Ioannis Deretzis, Viviana Scuderi, Cristiano Calabretta, Filippo Giannazzo, Marcin Zielinski, et al. New approaches and understandings in the growth of cubic silicon carbide. *Materials*, 14(18):5348, 2021.

- [9] Hosung Seo, Abram L Falk, Paul V Klimov, Kevin C Miao, Giulia Galli, and David D Awschalom. Quantum decoherence dynamics of divacancy spins in silicon carbide. *Nature communications*, 7(1):1–9, 2016.
- [10] Tommaso Fazio, Giuseppe Fisicaro, Ioannis Deretzis, Elisabetta Paladino, and Antonino La Magna. Computational study of the silicon vacancy in 3c-sic and perspectives for quantum technologies. In *Materials Science Forum*, volume 1062, pages 309–314. Trans Tech Publ, 2022.
- [11] Abram L Falk, Bob B Buckley, Greg Calusine, William F Koehl, Viatcheslav V Dobrovitski, Alberto Politi, Christian A Zorman, Philip X-L Feng, and David D Awschalom. Polytype control of spin qubits in silicon carbide. *Nature communications*, 4(1):1–7, 2013.
- [12] Paolo Giannozzi, Stefano Baroni, Nicola Bonini, Matteo Calandra, Roberto Car, Carlo Cavazzoni, Davide Ceresoli, Guido L Chiarotti, Matteo Cococcioni, Ismaila Dabo, et al. Quantum espresso: a modular and open-source software project for quantum simulations of materials. *Journal of physics: Condensed matter*, 21(39):395502, 2009.
- [13] Chris J Pickard and Francesco Mauri. All-electron magnetic response with pseudopotentials: Nmr chemical shifts. *Physical Review B*, 63(24):245101, 2001.
- [14] Jérémie Lefèvre, Jean-Marc Costantini, Didier Gourier, Stéphane Esnouf, and Guillaume Petite. Characterization of a silicon-related defect detected by its excited triplet state in electron-irradiated 3c-sic. *Physical Review B*, 83(7):075201, 2011.
- [15] Viktor Ivády, Joel Davidsson, Nguyen Tien Son, Takeshi Ohshima, Igor A Abrikosov, and Adam Gali. Identification of si-vacancy related room-temperature qubits in 4 h silicon carbide. *Physical Review B*, 96(16):161114, 2017.
- [16] Michel Bockstedte, Matthias Heid, and Oleg Pankratov. Signature of intrinsic defects in sic: Ab initio calculations of hyperfine tensors. *Physical Review B*, 67(19):193102, 2003.
- [17] Charles P Slichter. *Principles of magnetic resonance*, volume 1. Springer Science & Business Media, 2013.



- [18] E Paladino, YM Galperin, G Falci, and BL Altshuler. 1/f noise: Implications for solid-state quantum information. *Reviews of Modern Physics*, 86(2):361, 2014.
- [19] G Falci, A D’arrigo, A Mastellone, and E Paladino. Initial decoherence in solid state qubits. *Physical review letters*, 94(16):167002, 2005.
- [20] J Bergli, Yu M Galperin, and BL Altshuler. Decoherence in qubits due to low-frequency noise. *New Journal of Physics*, 11(2):025002, 2009.
- [21] Wen Yang and Ren-Bao Liu. Quantum many-body theory of qubit decoherence in a finite-size spin bath. *Physical Review B*, 78(8):085315, 2008.
- [22] Grzegorz Chalasinski and Malgorzata M Szczesniak. Origins of structure and energetics of van der waals clusters from ab initio calculations. *Chemical Reviews*, 94(7):1723–1765, 1994.
- [23] Krisztián Szász, Tamás Hornos, Martijn Marsman, and Adam Gali. Hyperfine coupling of point defects in semiconductors by hybrid density functional calculations: The role of core spin polarization. *Physical Review B*, 88(7):075202, 2013.
- [24] Viktor Ivády, Tamás Simon, Jeronimo R Maze, IA Abrikosov, and Adam Gali. Pressure and temperature dependence of the zero-field splitting in the ground state of nv centers in diamond: A first-principles study. *Physical Review B*, 90(23):235205, 2014.
- [25] Birgit Krummheuer, Vollrath Martin Axt, and Tilmann Kuhn. Theory of pure dephasing and the resulting absorption line shape in semiconductor quantum dots. *Physical Review B*, 65(19):195313, 2002.
- [26] Fattah Sakuldee and Łukasz Cywiński. Characterization of a quasistatic environment with a qubit. *Physical Review A*, 99(6):062113, 2019.
- [27] Jianqi Xi, Bin Liu, Yanwen Zhang, and William J Weber. Ab initio study of point defects near stacking faults in 3c-sic. *Computational Materials Science*, 123:131–138, 2016.
- [28] John P Perdew, Kieron Burke, and Matthias Ernzerhof. Generalized gradient approximation made simple. *Phys. Rev. Lett.*, 77(18):3865, 1996.

- [29] David Vanderbilt. Soft self-consistent pseudopotentials in a generalized eigenvalue formalism. *Phys. Rev. B*, 41(11):7892, 1990.
- [30] DR Hamann, M Schlüter, and C Chiang. Norm-conserving pseudopotentials. *Physical Review Letters*, 43(20):1494, 1979.
- [31] Hendrik J Monkhorst and James D Pack. Special points for brillouin-zone integrations. *Phys. Rev. B*, 13(12):5188, 1976.
- [32] Nicola Varini, Davide Ceresoli, Layla Martin-Samos, Ivan Girotto, and Carlo Cavazzoni. Enhancement of dft-calculations at petascale: nuclear magnetic resonance, hybrid density functional theory and car-parrinello calculations. *Computer Physics Communications*, 184(8):1827–1833, 2013.
- [33] He Ma, Marco Govoni, and Giulia Galli. Pyzfs: A python package for first-principles calculations of zero-field splitting tensors. *Journal of Open Source Software*, 5(47):2160, 2020.
- [34] Christoph Freysoldt, Blazej Grabowski, Tilmann Hickel, Jörg Neugebauer, Georg Kresse, Anderson Janotti, and Chris G Van de Walle. First-principles calculations for point defects in solids. *Reviews of modern physics*, 86(1):253, 2014.
- [35] Michel Bockstedte, Alexander Mattausch, and Oleg Pankratov. Ab initio study of the migration of intrinsic defects in 3c-sic. *Physical Review B*, 68(20):205201, 2003.
- [36] Takuji Oda, Yanwen Zhang, and William J Weber. Study of intrinsic defects in 3c-sic using first-principles calculation with a hybrid functional. *The Journal of chemical physics*, 139(12):124707, 2013.
- [37] L Torpo, Risto M Nieminen, KE Laasonen, and S Pöykkö. Silicon vacancy in sic: a high-spin state defect. *Applied physics letters*, 74(2):221–223, 1999.
- [38] Adolf Schöner, Michael Krieger, Gerhard Pensl, Masayuki Abe, and Hiroyuki Nagasawa. Fabrication and characterization of 3c-sic-based mosfets. *Chemical Vapor Deposition*, 12(8-9):523–530, 2006.

- [39] J Isoya, T Umeda, N Mizuochi, NT Son, Erik Janzén, and T Ohshima. Epr identification of intrinsic defects in sic. *physica status solidi (b)*, 245(7):1298–1314, 2008.
- [40] Mt Wagner, NQ Thanh, NT Son, WM Chen, Erik Janzén, PG Baranov, EN Mokhov, Christer Hallin, and JL Lindström. Ligand hyperfine interaction at the neutral silicon vacancy in 4h-and 6 h- sic. *Physical Review B*, 66(15):155214, 2002.
- [41] WM Witzel and S Das Sarma. Quantum theory for electron spin decoherence induced by nuclear spin dynamics in semiconductor quantum computer architectures: Spectral diffusion of localized electron spins in the nuclear solid-state environment. *Physical Review B*, 74(3):035322, 2006.
- [42] Wang Yao, Ren-Bao Liu, and LJ Sham. Theory of electron spin decoherence by interacting nuclear spins in a quantum dot. *Physical Review B*, 74(19):195301, 2006.
- [43] SK Saikin, Wang Yao, and LJ Sham. Single-electron spin decoherence by nuclear spin bath: Linked-cluster expansion approach. *Physical Review B*, 75(12):125314, 2007.
- [44] Arthur Schweiger and Gunnar Jeschke. *Principles of pulse electron paramagnetic resonance*. Oxford University Press on Demand, 2001.
- [45] Mykyta Onizhuk, Kevin C Miao, Joseph P Blanton, He Ma, Christopher P Anderson, Alexandre Bourassa, David D Awschalom, and Giulia Galli. Probing the coherence of solid-state qubits at avoided crossings. *PRX Quantum*, 2(1):010311, 2021.
- [46] DI Hoult and NS Ginsberg. The quantum origins of the free induction decay signal and spin noise. *Journal of Magnetic Resonance*, 148(1):182–199, 2001.
- [47] S Bengtsson, Esben Witting Larsen, D Kroon, S Camp, M Miranda, CL Arnold, A L’Huillier, KJ Schafer, MB Gaarde, L Rippe, et al. Space-time control of free induction decay in the extreme ultraviolet. *Nature Photonics*, 11(4):252–258, 2017.

- [48] H Okumura, H Itoh, I Nashiyama, S Yamasaki, S Misawa, and S Yoshida. Characterization of 3c-sic epilayers by pulsed electron spin resonance. *Materials Science and Engineering: B*, 11(1-4):31–34, 1992.
- [49] Elliott Fraval, MJ Sellars, and JJ Longdell. Dynamic decoherence control of a solid-state nuclear-quadrupole qubit. *Physical review letters*, 95(3):030506, 2005.
- [50] Mykyta Onizhuk and Giulia Galli. Pycce: A python package for cluster correlation expansion simulations of spin qubit dynamics. *Advanced Theory and Simulations*, 4(11):2100254, 2021.